ADVANCING EARTH AND SPACE SCIENCES

Geophysical Research Letters

RESEARCH LETTER
10.1029/2023GL105243

Observations of Ocean Surface Wave Attenuation in Sea Ice Using Seafloor Cables

Madison M. Smith[1], Jim Thomson[2], Michael G. Baker[3], Robert E. Abbott[3], and Jake Davis[2]

[1]Woods Hole Oceanographic Institution, Woods Hole, MA, USA, [2]Applied Physics Laboratory, University of Washington, Seattle, WA, USA, [3]Sandia National Laboratories, Albequerque, NM, USA

Key Points:

- Seafloor fiber optic cables can be used to quantify surface waves in seasonally sea ice-covered oceans
- High spatial-resolution wave observations may be used to study wave attenuation in ice at much finer resolution than previously possible
- The rapid evolution of the location and strength of attenuation serves as proxy for the evolution of ice itself

Correspondence to:

M. M. Smith,
madisonmsmith@whoi.edu

Citation:

Smith, M. M., Thomson, J., Baker, M. G., Abbott, R. E., & Davis, J. (2023). Observations of ocean surface wave attenuation in sea ice using seafloor cables. *Geophysical Research Letters*, *50*, e2023GL105243. https://doi.org/10.1029/2023GL105243

Received 28 JUN 2023
Accepted 22 SEP 2023

Author Contributions:

Conceptualization: Madison M. Smith, Jim Thomson
Data curation: Madison M. Smith, Michael G. Baker
Formal analysis: Madison M. Smith
Funding acquisition: Madison M. Smith, Jim Thomson
Investigation: Madison M. Smith
Methodology: Madison M. Smith, Jim Thomson, Jake Davis
Project Administration: Robert E. Abbott
Resources: Jim Thomson, Michael G. Baker, Robert E. Abbott
Software: Madison M. Smith
Validation: Madison M. Smith
Visualization: Madison M. Smith
Writing – original draft: Madison M. Smith

Abstract The attenuation of ocean surface waves during seasonal ice cover is an important control on the evolution of Arctic coastlines. The spatial and temporal variations in this process have been challenging to resolve with conventional sampling using sparse arrays of moorings or buoys. We demonstrate a novel method for persistent observation of wave-ice interactions using distributed acoustic sensing (DAS) along existing seafloor fiber optic telecommunications cables. DAS measurements span a 36-km cross-shore cable on the Beaufort Shelf from Oliktok Point, Alaska. DAS optical sensing of fiber strain-rate provides a proxy for seafloor pressure, which we calibrate with wave buoy measurements during the ice-free season (August 2022). We apply this calibration during the ice formation season (November 2021) to obtain unprecedented resolution of variable wave attenuation rates in new, partial ice cover. The location and strength of wave attenuation serve as proxies for ice coverage and thickness, especially during rapidly evolving events.

Plain Language Summary Coasts globally are susceptible to erosion by ocean waves. In the Arctic, sea ice near the coast can serve as protection for much of the year. It is particularly challenging to measure waves and ice in this environment, which is necessary to understand the degree of buffering and project future changes. Typical ways of observing waves (e.g., buoys and underwater moorings) have lower success in coastal ice. We show a new way to observe waves and ice in these coastal regions using cables at the seabed deployed for internet connection. With the use of an instrument called an interrogator on shore, fibers in these cables can act like a series of hundreds of wave buoys. This allows us to see that waves are reduced at a variable rate throughout the ice. There are significant opportunities to learn more about the coastal Arctic using this novel technology and method.

1. Introduction

Sea ice attenuates surface wave energy through a variety of scattering and dissipative processes (e.g., Squire, 2019). Wave attenuation rates typically increase with frequency, with magnitude that varies as a function of ice type, coverage, and thickness (Meylan et al., 2018; Kohout et al., 2020; Rogers et al., 2021). Wave attenuation in new ice such as frazil and pancakes is typically dominated by dissipative processes (Kohout & Meylan, 2008) resulting in relatively low wave energy attenuation due to typically low thickness and concentration (Cheng et al., 2017; Hošeková et al., 2020). Progress in understanding wave attenuation in sea ice has been somewhat hindered by the limitation of observing apparent attenuation between widely spaced discrete wave measurement locations, such that it is challenging to spatially resolve the evolution of the processes (Thomson, 2022). For example, Hošeková et al. (2020) identify high attenuation rates within 500 m of an ice edge relative to the attenuation farther within the ice, but lack sufficient data to explain the phenomenon.

Landfast ice typically extends 5–20 km in the cross-shore direction in the coastal Arctic (Mahoney, 2018), and provides sufficient attenuation to buffer the coast from most wave energy (Hošeková et al., 2021). In the Alaskan Arctic, landfast ice is predominantly seasonal (Mahoney et al., 2014), with dramatic transitions at spring break-out and autumn freeze-up. The coastal system is then more exposed to ocean waves and heat in the absence of this ice (Barnhart et al., 2014). Understanding the seasonal transitions of landfast ice and annual exposure to waves is necessary to understand the degree of buffering and to project future changes in inundation and erosion.

Measurements of waves in the coastal Arctic are challenging not only during partially ice-covered seasons, but also during open water periods because of logistical challenges including the remote location and shallow water depths. Distributed acoustic sensing (DAS) of seafloor fiber optic cables is an emerging technology that offers a particularly appealing method for observing spatial and temporal changes in surface waves in remote

Writing – review & editing: Madison M. Smith, Jim Thomson, Michael G. Baker, Robert E. Abbott, Jake Davis

and seasonally ice-covered coastal environments. A DAS interrogator is connected to the end of an optical fiber to observe reflection of lasers off impurities in the glass, providing measurement of strain or strain-rate. Seafloor DAS (or ocean-bottom DAS, OBDAS) has previously been demonstrated to be capable of observing ocean surface waves (Lindsey et al., 2019; Williams et al., 2019), and methods are rapidly evolving for use quantifying a range of other oceanographic and geophysical processes (Baker & Abbott, 2022; Landrø et al., 2022; Wilcock et al., 2023). Measurements of such high spatial resolution are generally unprecedented in Polar regions.

This work demonstrates the quality and fidelity of DAS for ocean surface wave measurements in both open water and partially ice-covered periods in the coastal Arctic. Estimates of wave attenuation are both consistent with previously observed values and reveal new spatial variability. Attenuation observations can serve as an indication of changes in ice extent and thickness during rapidly evolving events. This can include ice loss (melting) and formation (freezing), as well as advection of sea ice.

2. Methods

2.1. DAS Observations

Observations presented here use DAS records from a cross-shore seafloor transect on the Beaufort Shelf. Data were recorded on dark fiber in a branch of a telecommunications cable owned by Quintillion and extending northwards from the landing site at Oliktok Point, Alaska, to a maximum of 37.4 km offshore (Figure 1a). The maximum water depth along this transect is 19.7 m, and the depth of cable burial is approximately 2 m until 16.1 km along-cable distance, then approximately 4 m beyond that. The fiber was interrogated using a Silixa iDAS interrogator during 1-week periods in 2021 and 2022; here we use data from November 2021 and August 2022 (Baker & Abbott, 2022). The interrogator measures cable strain-rate in units of nm/m/s. The cable is spliced at 16.1 km, coincident with the change in depth of fiber burial. Both the splice and depth-of-burial difference result in a change in sensitivity at this location.

Data was recorded in 15-s segments at a channel spacing or sampling distance of 2 m, with a 10-m gauge length and a sample rate of 1,000 Hz (1 kHz). The gauge length is the distance over which strain is integrated, and thus acts like a moving-average filter. Data records were concatenated to 1-hr segments and downsampled to 40 m and 2 Hz to reduce data volumes for this work, as 2 Hz should be sufficient to capture any ocean surface gravity wave signals that are observable at the seafloor over the range of water depths measured. Temporal downsampling was completed by transforming raw data to the frequency domain with a zero-padded 2N fft with $N = 3.6 \times 10^6$, which is then convolved with a zero-phase lowpass finite impulse response filter with cutoff frequency of 1 Hz. This is then transformed back to the time domain with every 500th sample extracted. We expect the gauge length to most significantly limit the observable wavelength, where 10 m wavelength (L) corresponds to a 2.5 s wave period (0.4 Hz) in deep water $\left(L = \frac{gT^2}{2\pi}\right)$.

Frequency-wavenumber analysis (Figure 2; following Baker & Abbott, 2022) calculated with 2D Fourier transforms of 20 Hz downsampled data at all 1,001 channels between 16 and 18 km along-cable distance suggests that DAS is a robust method for observing surface gravity waves in a variety of conditions. Examples from the open water period (Figure 2a) and during ice advance (Figure 2b) both show the dispersion of surface gravity waves. The surface gravity wave signal fades at higher frequencies during open water periods than during periods with sea ice. Further calibration can be used to retrieve quantification of waves from these signals.

2.2. Wave Buoy Measurements

A moored Surface Wave Instrument Float with Tracking (SWIFT) wave buoy (Thomson, 2012) (Figure 1b) was deployed 14 August–1 September 2022 to provide in situ surface wave comparison for the seafloor DAS. The buoy was deployed at 16.2 km along-cable distance (70.62°N, 150°W; orange point in Figure 1a), in approximately 12.6 m water depth. Waves are measured using a combination GPS and IMU receiver with a 12-min record at the top of each hour following the details in Thomson et al. (2018). Horizontal velocity vectors are decomposed into mean and wave orbital velocity components to infer wave energy spectra (Herbers et al., 2012). Spectra were processed up to 1 Hz, with bulk parameters of significant wave height (H_s) and energy-weighted wave period (T_e) calculated over 0.03–0.5 Hz to avoid the noise common in higher frequencies of observations

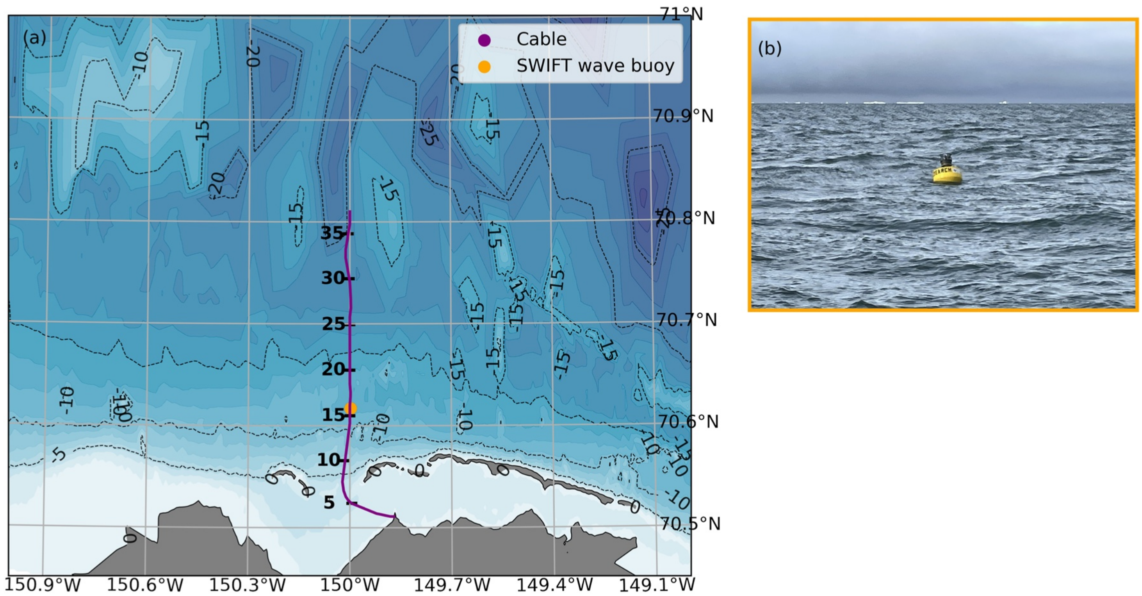

Figure 1. (a) Map of observations near Oliktok Point, Alaska, with the seafloor cable used for distributed acoustic sensing measurements in purple and Surface Wave Instrument Float with Tracking (SWIFT) wave buoy (August 2022) in orange. Black tick labels show along-cable distance in km. Background contours show bathymetry from NOAA navigation maps (Baker & Abbott, 2022) in meters. (b) Photo of a moored SWIFT wave buoy in open water.

(Thomson et al., 2021a). Significant wave height is defined as $H_s = 4\sqrt{\int E(f)\, df}$ and energy-weighted wave period is defined as $T_e = \frac{\int E(f) df}{\int E(f) \cdot f\, df}$.

2.3. Calculation of DAS Empirical Correction Factor

The measurement of strain-rate by DAS is used as a proxy for the seafloor pressure. In order to convert it to a spectrum that can be used to approximate wave parameters, we derive a frequency-dependent empirical correction factor for each channel (i.e., each location along the cable). The correction factor calculation uses all measurements from the open-water record 16–21 August 2022, when the SWIFT wave buoy was deployed concurrently. The calibration data set covers a relatively small range of wave heights (0–0.5 m) and periods

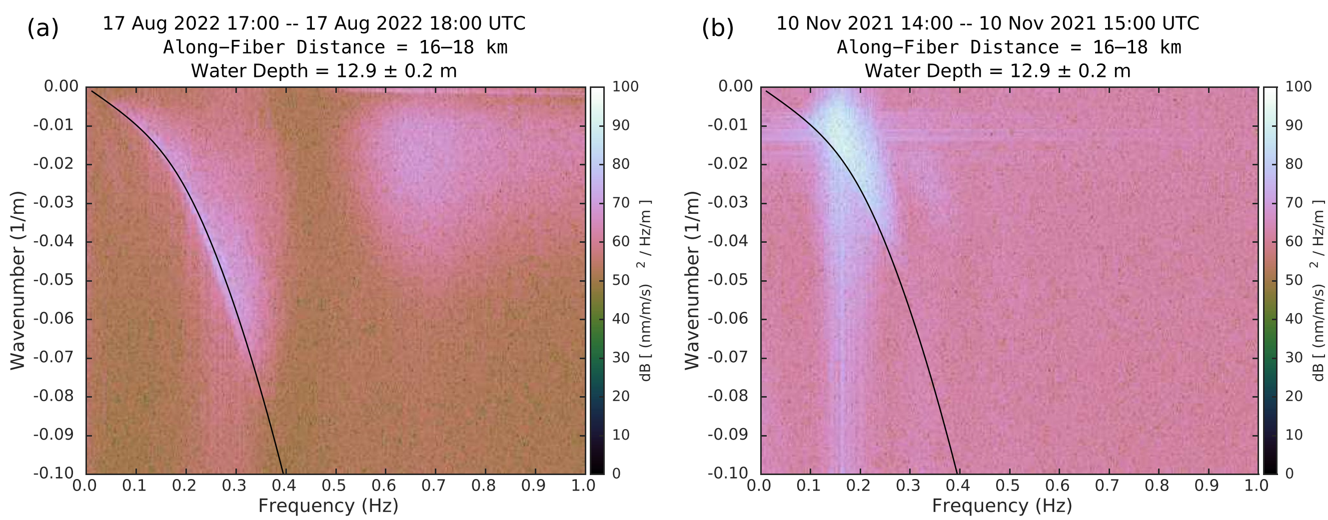

Figure 2. Frequency-wavenumber (f–k) plots using 1 hr of data at 1001 distributed acoustic sensing channels from 16 to 18 km along-fiber distance. Gravity wave dispersion curves (black lines) were calculated using the mean water column depth. Ocean gravity waves are observable both in panel (a) open water, 17 August 2022, 17:00–18:00 and (b) seasonal ice-cover, 10 November 2021, 14:00–15:00.

(2.5–3.5 s), where waves at similar shelf locations typically range from around 0–2 m seasonally (Thomson et al., 2020). In future experiments, calibration with data sets covering a larger range of likely conditions may result in a more robust calibration. Additionally, fiber strain has been found to be linearly related to the temperature of the cable (Sidenko et al., 2022). We expect this to have a small impact on the applicability of August calibration to the seasonal wave period due to the cable burial depth which should result in relatively slow temperature response to the variation of seafloor water temperature likely between −1.8 and 2°C (Thomson et al., 2020).

The empirical correction factor is calculated as a ratio of the power spectral density (PSD) of strain-rate and wave-driven seafloor pressure. We calculate the PSD of the raw strain-rate in each hour-long timestep using Welch's overlapped segment averaging estimator which uses a Hamming window of length 128 (64 s at 2 Hz) with 50% overlap. The SWIFT wave spectra from the same hour is identified, and a depth attenuation correction is applied to infer the expected seafloor pressure. The expected depth-dependent attenuation of wave energy is e^{-2kd}, where d is the depth, here defined as the sum of the water depth and the burial depth, and k is wavenumber from the linear surface gravity wave dispersion relation. Dividing the spectrum of seafloor pressure by the strain-rate spectrum gives an empirical correction factor (Figure A1). This is repeated for each timestep, and the empirical correction function is defined as the median of the correction factor for each timestep (Figure A2). The median is used rather than the mean as it results in a smoother transfer function for channels where there is more variability between timesteps, but this choice results in little difference in the resulting wave heights (<5% across all channels).

The process is repeated for all channels outside of the barrier islands (8–35 km along-cable distance). Empirical correction factors for all channels (Figure A3) especially vary at high frequencies, likely due to variability in seafloor type and coupling. While the location of the wave buoy used for calibration is up to 18 km away from the DAS channels analyzed, we assume here that the calibration data set is sufficiently long that spatial homogeneity can be assumed. The two most likely violations of the homogeneity assumption would be shoaling and local fetch-limited wind-wave generation. Shoaling is evaluated using the square root of the ratio of the group velocity between the deepest and shallowest sites. The resulting shoaling coefficient is close to unity (∼1.05) and thus does not cause much change in wave height along the cable. Fetch-limited generation can cause larger changes (up to 50%), but only causes gradual increases with the square root of distance (Thomson & Rogers, 2014).

2.4. Calculation and Evaluation of DAS Surface Wave Estimates

To derive corrected surface wave spectra from DAS observations, PSD of strain-rate (calculated using the Welch's method described in 2.3 above) are multiplied by the channel-specific frequency-dependent empirical correction factor (e.g., Figure A2) and divided by the depth-attenuation correction (e^{2kd}). Upper spectral cutoffs are subjectively determined at each timestep as an inflection point beyond which the spectral shape does not suggest surface waves and appears to be dominated by noise (Thomson et al., 2021a). The f–k spectra in Figure 2 clearly show when noise takes over as when energy is no longer concentrated along the dispersion curve, and demonstrate that the frequency at which this occurs varies during different time periods. Beyond the cutoff, spectra are fit with the canonical f^{-4} for high-frequencies waves (e.g., Liu, 1989; Figure A4). Not applying the spectral cutoff results in significantly greater wave height estimates—up to 2–3x larger during November ice advance—due to the observed noise in high frequencies, while not including the f^{-4} fit results an underestimation of wave heights—by up to 50% during the August open water period—as much of the wave energy is in these frequency bands (e.g., Figure A4).

Bulk wave characteristics are calculated from the corrected spectra using standard definitions over the frequency range of 0.03–0.5 Hz. The time series of bulk wave characteristics for the open-water calibration period is shown in Figure 3 (purple lines). Leave-one-out cross-validation is used to evaluate the methodology by estimating the out-of-sample error between bulk parameters derived from corrected DAS spectra and the buoy (orange lines). For all N coincident buoy and DAS observations during the 6-day observation period, a single time-step is excluded and the remaining N–1 observations are used to produce a median correction factor. The bulk parameter estimates are then evaluated on the left out test point. This gives root-mean-squared error (RMSE) = 0.10 m and R^2 = 0.84 for H_s, and RMSE = 0.65 s and R^2 = 0.52 for T_e for the channel closest to the buoy. Error is higher for T_e in part because larger values are more likely than for H_s, as well as that it is more sensitive to the higher frequencies that may not be as well resolved by seafloor DAS.

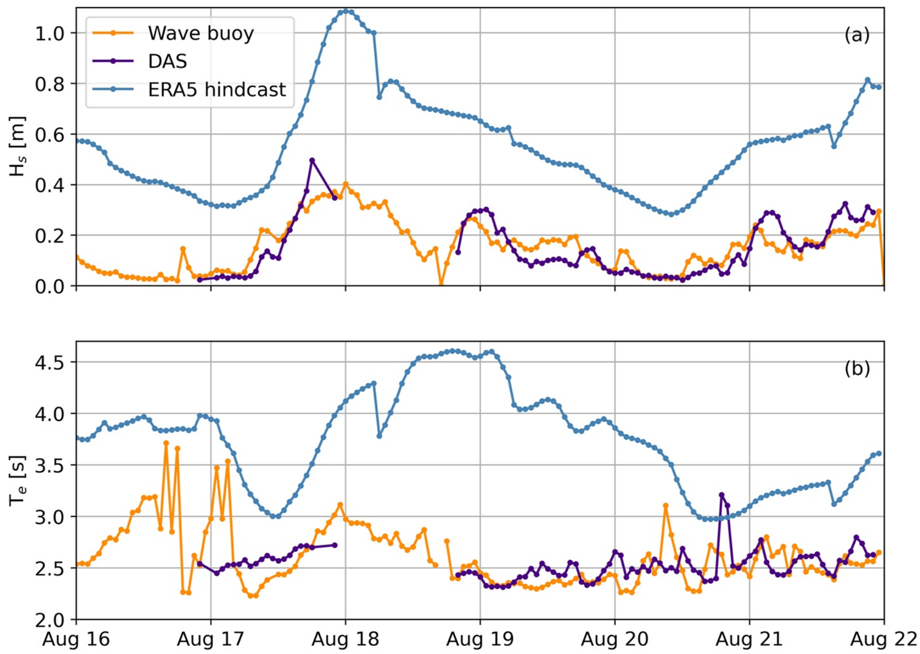

Figure 3. Time series of (a) significant wave height, (b) and energy-weighted wave period as measured by Surface Wave Instrument Float with Tracking wave buoy (orange), seafloor cable distributed acoustic sensing (DAS; purple; 16.2 km along-cable distance), and estimated by ERA5 hindcast model (blue). Buoy and ERA5 hindcast cover the period from August 16–22, 2022, while DAS observations are available for August 16 22:00–August 17 22:00 and August 18 20:00–August 21 22:00.

Wave spectra and bulk parameters can then also be calculated for other periods by applying the channel-specific empirical correction factor, including the November 2021 observation period presented here.

2.5. Wave Attenuation Rates

Wave attenuation by sea ice as a function of frequency, $\alpha(f)$, is calculated between two points (denoted by subscripts 1 and 2) as

$$\alpha(f) = \frac{1}{\Delta x} \ln \frac{E_1(f)}{E_2(f)} \tag{1}$$

where $E(f)$ is the spectral wave energy as a function of frequency and Δx is the distance between points 1 and 2. A bulk attenuation can also be calculated by using the bulk wave height (H_s) in place of frequency-dependent wave energy. The difference between a height attenuation rate and an energy attenuation rate is simply a factor of 2, because energy E depends on H^2. Attenuation calculated using wave height is most common and easily comparable with literature values, and the upper frequency cutoff used in the calculation avoids the known rollover at high frequencies in ice associated with noise (Thomson et al., 2021). We also show attenuation values at 0.1 and 0.2 Hz (× and + in Figure 4). We calculate the attenuation at 200 m intervals by averaging together attenuation results calculated using all wave estimates within a 4 km region. This produces smoother and more realistic attenuation results than from using individual spectra, but still captures the high spatial variability.

3. Results

3.1. Waves in Open Water, August 2022

Time series of bulk wave parameters during the open water observation period in August 2022 from both observational data sets are shown in Figure 3. The sea state was characterized by wind sea with energy-weighted periods (T_e) of 2.3–3.5 s measured by both the SWIFT wave buoy and the DAS channel closest to the buoy location. Wave heights peaked late on August 17 into early August 18. Peak wave heights of over 0.4 m were measured

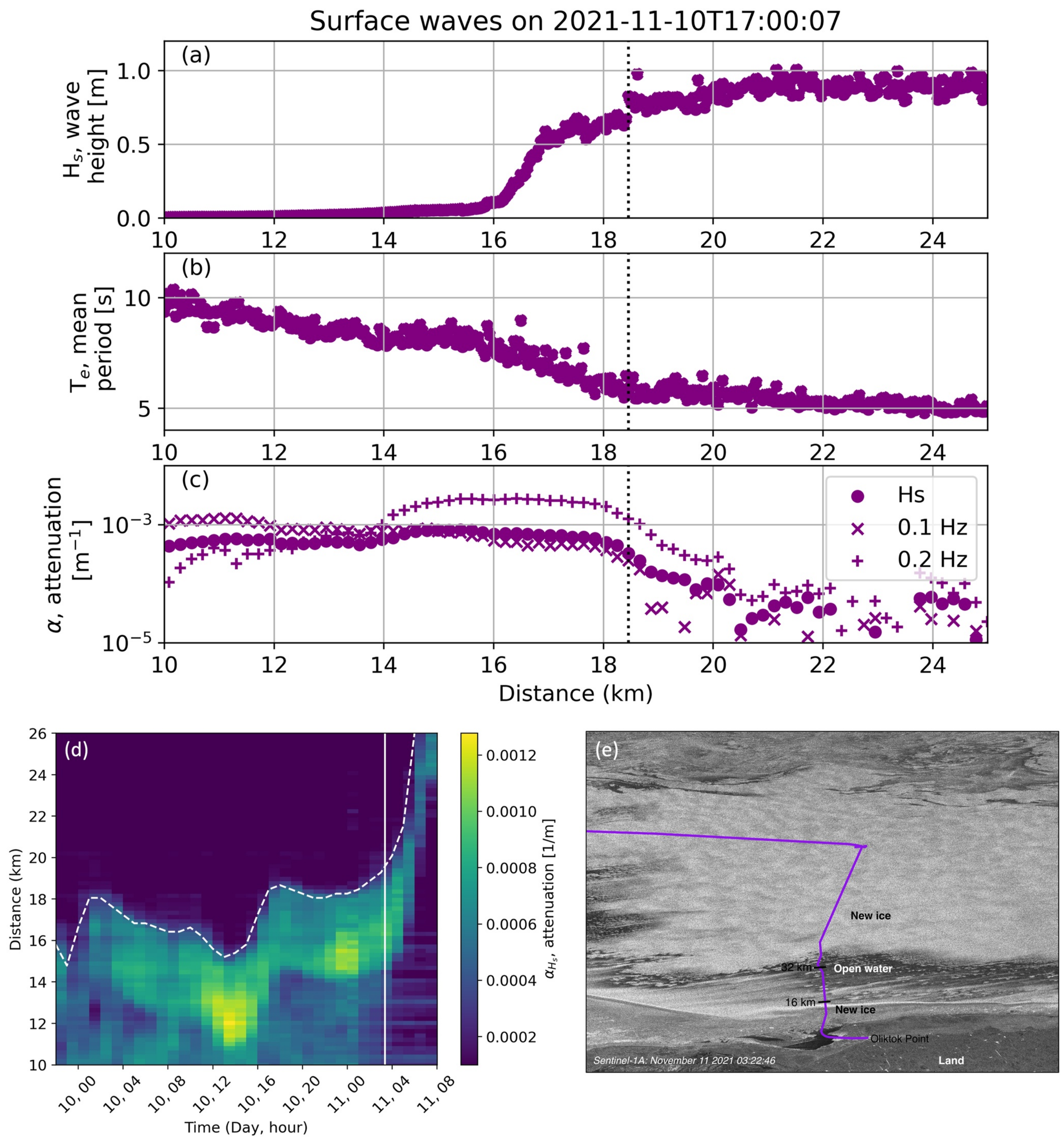

Figure 4. Wave parameters during November 2021 ice advance, where panels (a–c) shows along-cable estimates from a cross-section with partial ice cover on 10 November 2021, 17:00 for: (a) significant wave height, (b) energy-weighted mean wave period, and (c) wave attenuation rates. Wave attenuation is shown for significant wave height (circles), and at 0.1 Hz (x's) and 0.2 Hz (+'s), which bracket the range of mean wave periods observed (5–10 s; (c)). The dotted vertical line suggests the inferred location of the ice edge based on a bulk wave height attenuation rate of 3×10^{-4} m^{-1}. (d) Map of bulk wave height attenuation from November 9, 22:00 – November 11, 08:00, from 10 to 26 km along-cable distance. Dark blue suggests near-zero attenuation likely associated with open water. Green-yellow corresponding to higher attenuation rates suggest the presence of sea ice, where the dashed white line denotes the approximate ice edge associated with attenuation of greater than 3×10^{-4} m^{-1}. Vertical white line corresponds to time of synthetic aperature radar backscatter in (e) from November 11, 03:22, which suggests new ice (lower backscatter; white) to approximately 18 km along-cable distance. Black ticks correspond to 16 and 32 km along-cable distance. The full cable path is shown in purple, but observations only extend to 37.4 km along-cable distance (Section 2.1). Copernicus Sentinel data 2021 retrieved from ASF DAAC 18 May 2023, processed by ESA.

by the SWIFT wave buoy, while wave heights were somewhat overestimated by DAS at around 0.5 m at August 17 18:00. A gap in the DAS record from August 17 23:00–August 18 19:00 missed the remainder of the event. Wave directions during the full buoy deployment period (not shown) suggest that waves are typically from the NE and directed onshore, approximately perpendicular to the cable route. Quality of wave height retrievals from DAS do not seem to be explained by direction, as the difference does not significantly correlate with relative wave direction. During the open water period, energy observed by DAS in the surface wave frequencies is concentrated along the dispersion curve (Figure 2a).

We also compare wave measurements from both methods with bulk wave parameters provided by the European Centre for Medium-Range Weather Forecasts Reanalysis v5 (ERA5) hindcast product (Hersbach et al., 2020). The waves from this reanalysis have already been shown to be inaccurate during seasonal transitions, when the hindcast lacks the necessary resolution (Hošeková et al., 2021). The native grid resolution of 31 km cannot be expected to capture on-shelf processes, though there is some representation of sub-grid bathymetry as "obstructions" that should be especially important for transformation of longer waves (Bidlot, 2012). Still, the ERA5 products are being used to assess coastal exposure in Alaskan Arctic regions given the dearth of other sufficient data (e.g., Cohn et al., 2022; Hošeková et al., 2021), and thus we include it here for completeness. Waves are significantly overestimated by the hindcast (blue line in Figure 3), with significant wave heights double that observed by the wave buoy during the peak wave event and more than 4x larger during low-wave periods. The measurements from the DAS show significant improvement in capturing wave parameters compared to the hindcast. Throughout a range of wave conditions typical of the open water season, seafloor cable DAS can provide a high-fidelity method for capturing nearshore wave forcing and subsequent coastal wave exposure (e.g., Hošeková et al., 2021).

3.2. Wave Attenuation During Fall Ice Advance, November 2021

DAS measurements during the week of 10 November 2021, were coincident with the advance of new landfast ice over the cable near Oliktok Point (Baker & Abbott, 2022). We focus our analysis on distances from 10 to 25 km along-cable due to signal-to-noise issues outside that range. During this period, wave energy is concentrated along the dispersion curve at lower frequencies and attenuated at high frequencies (Figure 2b). Additionally, waves are shifted slightly off the classic dispersion relation, indicating a shift to a shorter wavenumber which could result from directional filtering or refraction (Wahlgren et al., 2023).

A spatial cross-section of wave retrievals from 10 November 17:00 (Figures 4a–4c) demonstrates characteristics of the spatial patterns of wave evolution in new, autumn sea ice. This is consistent with Sentinel-1A synthetic aperature radar imagery from earlier on the same date (11 November 03:22, Figure 4e) which shows new ice formation both inshore of approximately 18 km along-cable distance and beyond 35 km (outside of the measurement range), with a patch of open water between. ERA5 suggests wind speeds of around 12 m/s in the early hours of November 10, providing sufficient energy for shoreward wave generation in the open water patch. Wave heights and energy-weighted wave periods show spatial variability with distance from offshore to onshore that is characteristic of wave attenuation in sea ice. Wave heights decrease notably over this distance, peaking at a height of 1.0 m offshore and approaching the lower observable limit (<0.05 m) near 12 km. Energy-weighted periods are approximately constant around 5 s from 20 to 25 km along-cable distance, where we begin to see a shift toward longer periods (lower frequencies) with a peak of around 10 s. This increase in mean wave period is characteristic of waves in ice (Squire & Moore, 1980; Waseda et al., 2022). The strongest change is spatially aligned with the steepest change in wave height.

The example cross-section from 10 November 17:00, shows a rapid increase in attenuation rates around 18.5 km, which we expect to be associated with young ice formation (Figure 4c). Attenuation of bulk wave height reaches a maximum of 8.1×10^{-4} approximately 15 km along-cable distance. Attenuation rates are in general higher near the ice edge, and the spectral attenuation at 0.2 Hz reaches a maximum of 2.8×10^{-3}, and remains elevated near this value from approximately 15-18 km. The attenuation values are most similar around 12–14 km distance, where wave energy in the high frequency bands has been significantly attenuated, and remaining energy is dominantly in the lower frequency bands. The spectral attenuation at 0.1 Hz becomes greater than that at 0.2 Hz around 14 km, where wave heights are small and little high-frequency wave energy remains. In agreement with prior work (Hošeková et al., 2020), this suggests that the spectral attenuation rates evolve through two-way coupling within heterogeneous wave-ice fields. Constant spectral attenuation rates as a function of ice type or thickness

10.1029/2023GL105243

may not be sufficient over large distances. Wave heights are notably small closer to shore (10–14 km), but still show bulk attenuation rates that are characteristic of new frazil and pancake ice ($\sim 5 \times 10^{-4}$ m^{-1}) (Hošeková et al., 2020; Voermans et al., 2019). Near-zero attenuation rates beyond 20.3 km suggest open water offshore of this location.

For the purposes of subsequent analysis, we use the bulk attenuation to define an "ice edge" at the first incidence of attenuation greater than 3×10^{-4} m^{-1}, indicated by a vertical dashed line in the cross-section in Figures 4a–4c. We can see that there are minor reductions in wave height and period prior to this location that indicate presence of some ice, likely of low concentration and/or very thin. Multiple definitions of the ice edge may be appropriate for different applications.

Mapping bulk wave attenuation as a function of time and space reveals aspects of the spatial evolution of the ice (Figure 4d). In general, we suggest that the magnitude of attenuation is correlated primarily with ice concentration and thickness, and the slope of lines in time and space indicate the advection speed of the ice. Using the defined "ice edge" cutoff, we map the extent of sea ice (dashed white line in Figure 4d). The ice edge initially migrates shoreward, with the extent shifting approximately 2.7 km over the 11 hr from November 10 02:00-13:00. This corresponds to an approximate velocity of 0.072 m/s. Previous work has suggested that sea ice velocity follows the wave- and wind-driven flow at the surface (Lund et al., 2018). As such, we expect that the translation of the ice edge may be associated with wave-driven Stokes drift. For comparison, we calculate the anticipated Stokes drift $\bar{u}_s$ over this period using the average bulk wave parameters incident on the ice edge:

$$\bar{u}_s = \frac{2\, g\, \pi^3 H_s^2}{g\, T_e^3} \tag{2}$$

giving an approximate velocity of 0.069 m/s at the ice edge. This will of course decay with decreasing H_s and increasing T_e farther into the ice, so it may be insufficient to explain the ice transport.

Another mechanism for ice transport is a gradient in wave radiation stress (i.e., momentum flux), which has been shown to force motion along an ice edge (Thomson et al., 2021b). This mechanism is explicitly related to the wave attenuation rate, because that sets the gradient of the radiation stress (and thus the transfer of momentum from the waves to the ice). For the across ice (shoreward) component and waves normally incident, the expected speed $\bar{u}$ is

$$\bar{u} = H_0 e^{-\alpha x} \sqrt{\frac{\alpha g}{8 C_D}}. \tag{3}$$

Using an ice-ocean drag coefficient of $C_D = 8 \times 10^{-3}$ and bulk attenuation of $\alpha = 1 \times 10^{-4}$, this similarly gives an approximate velocity estimate of 0.1 m/s. This shoreward velocity, in addition to the Stokes drift and direct wind drift, likely results in compaction of the ice edge into higher concentration and thicker frazil or pancake layer (e.g., Wadhams, 1983). The compacted ice, in turn, is likely the cause of a local maxima in wave attenuation rate at the ice edge.

From November 10 13:00 and onwards into November 11, the ice edge nearly uniformly advances offshore. This evolution suggests a combination of offshore ice motion and additional formation of thin, new ice (e.g., 04:00–08:00 on November 11). The ice advance signal is consistent with the results of Baker and Abbott (2022) and Castro et al. (2023), who used the same data set to suggest that changes in DAS signal can be used to resolve spatial evolution of ice advance not captured by other methods (e.g., satellite products). After November 11 08:00, wave signals across the cable approach the lower observable limit, presumably associated with widespread ice advance and reduction of incident waves. ERA5 suggests wind speeds decline from 12 m/s to approximately 7.5 m/s over the period shown in Figure 4d.

4. Conclusions

Using a novel surface wave observation method, we observe high spatial variability of wave attenuation rates in new, autumn sea ice. Wave attenuation by thin, new landfast ice is relatively gradual, leaving open the possibility for incomplete attenuation and coastal impacts during fall storms. The attenuation rates were similar to those previously observed during autumn evolution off the shelf (Cheng et al., 2017; Hošeková et al., 2020), in the range of 3–8 × 10^{-4} m^{-1}. The results here suggest that higher attenuation rates previously observed near the ice-edge

10.1029/2023GL105243

may be a result of wave-ice interactions leading to ice compaction and increased thickness. Such high-resolution estimates of wave attenuation will contribute to better understanding the range of wave attenuation coefficients appropriate for different ice types and thicknesses, and implementation in coupled wave-sea ice models.

Seafloor DAS is demonstrated to be a particularly promising method for observing waves in challenging coastal environments, such as the seasonally ice-covered coastal Arctic. We expect this technology to be especially useful during periods of rapid change, including freeze-up (as shown here) and break-out in the spring. Ice break-out is particularly challenging to capture with typical methods due to its episodic nature with rapidly evolving spatial gradients, and may be well-suited to observation with DAS. Additionally, DAS can provide a non-invasive manner to measure wave exposure of the Arctic coastlines, which is of high utility for understanding rapid erosion rates. Currently, there are only a few seafloor telecommunication cables in the Arctic available for such purposes. The opportunities are likely to expand with proposed projects in the coming years, and deployment of shorter cable runs for scientific use may be regionally possible, though costly.

Many unknowns remain in the signal response of seafloor DAS and best practices for retrieval of surface wave parameters. Efforts are currently underway to derive physically based retrieval methods, as well as to understand the implications of empirical calibration methods and best practices using a collection of DAS data sets from different locations with a range of wave conditions. Currently, an empirical calibration is likely necessary for most observations due to unquantified factors in cable strain response to seafloor pressure (seabed substrate, compliance of the cable, etc.). Nonetheless, the observations presented here suggest that empirical calibration methods result in realistic wave spectra and bulk wave characteristics that are of use for monitoring and process understanding.

Appendix A: Additional Figures for Methods to Derive Empirical DAS Correction Factor and Calculate Wave Parameters

The following figures provide additional demonstration of the methods utilized to derive empirical DAS correction factors for calculation of surface wave parameters. Figure A1 shows an example calculation of the empirical correction factor for the DAS channel closest to the SWIFT wave buoy deployment location (channel 7960).

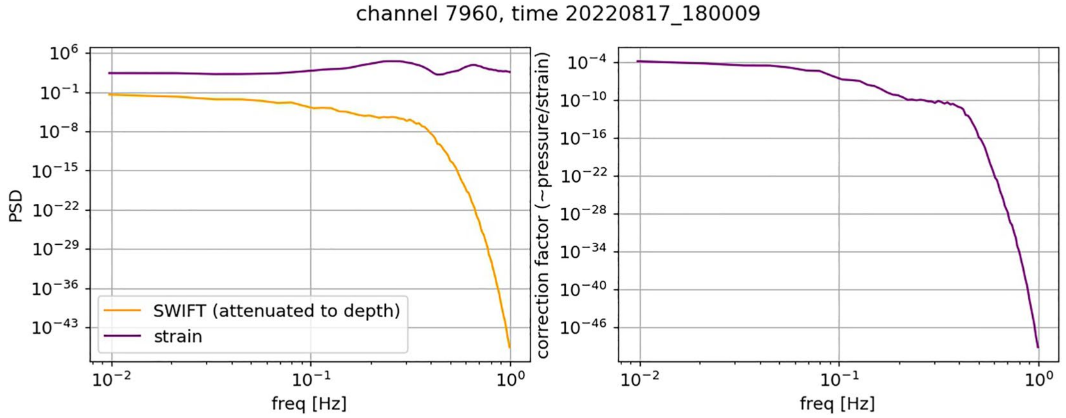

Figure A1. Example calculation of empirical correction factor for channel 7,960 (16.2 km along-cable distance) at 18:00 on 17 August 2022. Left panel shows power spectral density of raw distributed acoustic sensing strain-rate (purple) and inferred seafloor pressure from Surface Wave Instrument Float with Tracking (orange). Right panel shows the empirical correction factor calculated as a ratio of the PSDs.

10.1029/2023GL105243

Figure A2 shows calculation of the median empirical correction factor from the ratio of seafloor pressure to strain-rate at each timestep.

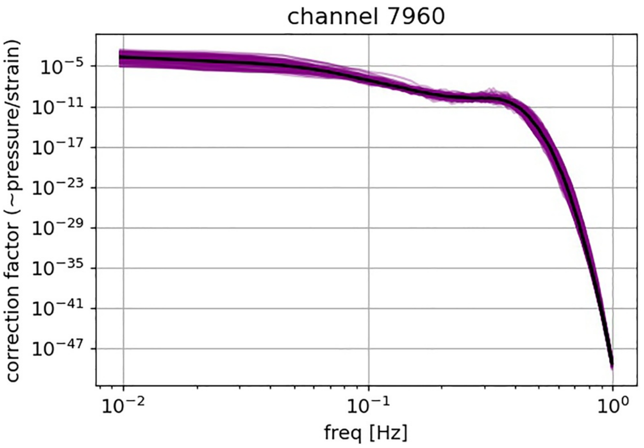

Figure A2. All empirical correction factors for channel 7,960 (16.2 km along-cable distance, as in example in Figure A1). Black line indicates the median value that is used as the channel-specific empirical correction factor in subsequent analysis.

Figure A3 shows empirical correction factors from all channels, where the high-frequency slope is higher (steeper) for channels in deeper water.

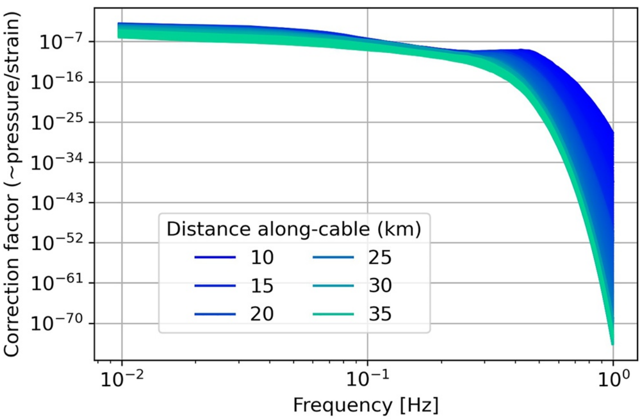

Figure A3. Empirical correction factors for all channels from 8 to 35 along-cable distance, determined as the median of all time steps (Figure A2). Colors indicate the along-cable distance, with blue at 8 km to green at 35 km.

Figure A4 demonstrates the correction of surface wave spectra derived from DAS for high-frequency noise.

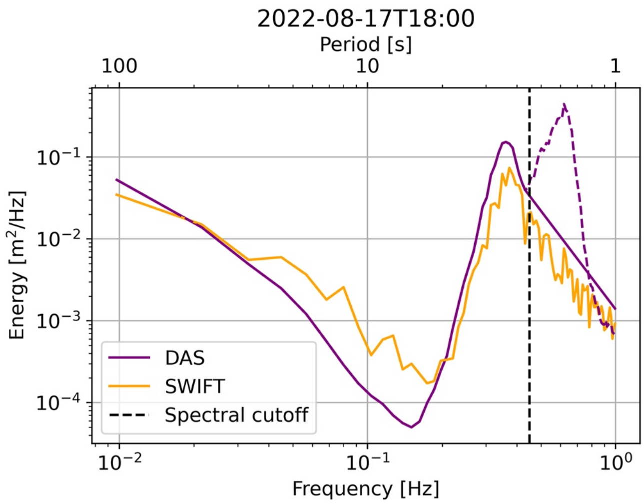

Figure A4. Example of methods for correcting high-frequency noise in wave spectra (see Section 2.4). An inflection point is determined empirically from original DAS-derived spectra (dashed purple line), here around 0.45 Hz. Beyond that, corrected spectra (solid purple line) is fit with the canonical f^{-4} slope for high-frequency waves. Observed wave spectra from Surface Wave Instrument Float with Tracking (orange) shows improved agreement with the corrected spectra. Note that the secondary peak at 0.7 Hz may be evidence of acoustic harmonics from ocean surface gravity waves (e.g., Ardhuin et al., 2013), which will be explored with this data set in future work.

Figure A5 shows an example of the calculation of spectral wave attenuation using wave spectra from two channel locations.

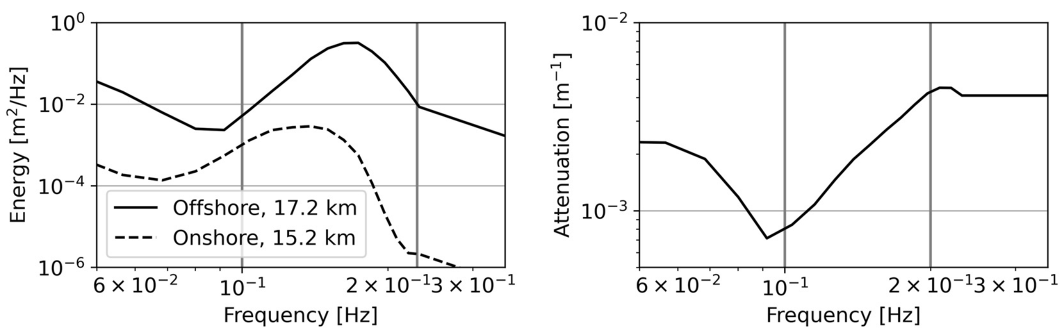

Figure A5. Example calculation of spectral attenuation following Equation 1. DAS-derived wave spectra from 17.2 to 15.2 km along-cable distance (left) are used to calculate attenuation rate (right). Vertical lines correspond to the frequency values shown in Figure 4c (×'s and +'s).

Data Availability Statement

Data sets of derived ocean surface gravity wave parameters are archived with the Arctic Data Center at https://doi.org/10.18739/A2PK0736C (Smith et al., 2023). The DAS data recorded by the Cryosphere/Ocean Distributed Acoustic Sensing (CODAS) Experiment for the November 2021 period are archived at Open Energy Data Initiative (mhkdr.openei.org/submissions/438). Code to produce wave DAS-derived wave products is available at github.com/smithmadisonm/DAS-surface-wave-processing. Preliminary data products from the SWIFT wave buoy are available online at http://faculty.washington.edu/jmt3rd/SWIFTdata/DynamicDataLinks.html, where the buoy deployed here was SWIFT 18.

Acknowledgments

MS and JT were funded by NSF EAGER Grants OPP 2214651 and 2215134. MB and RA were supported by the Laboratory Directed Research and Development program at Sandia National Laboratories, a multimission laboratory managed and operated by National Technology and Engineering Solutions of Sandia LLC, a wholly owned subsidiary of Honeywell International Inc. for the U.S. Department of Energy's National Nuclear Security Administration under contract DE-NA0003525. We thank Quintillion for fiber access and Silixa, LLC, for data collection and analysis advice. We thank Dr. Emily Eidam and the crew of the R/V Ukpik including Mike Fleming for assistance with deployment of SWIFT buoy. We thank Hannah Glover and Meagan Wengrove for useful discussion on methods for empirical calibration of surface wave measurements from seafloor DAS.

References

Ardhuin, F., Lavanant, T., Obrebski, M., Marié, L., Royer, J.-Y., d'Eu, J.-F., et al. (2013). A numerical model for ocean ultra-low frequency noise: Wave-generated acoustic-gravity and Rayleigh modes. *Journal of the Acoustical Society of America*, *134*(4), 3242–3259. https://doi.org/10.1121/1.4818840

Baker, M. G., & Abbott, R. E. (2022). Rapid refreezing of a marginal ice zone across a seafloor distributed acoustic sensor. *Geophysical Research Letters*, *49*(24), e2022GL099880. https://doi.org/10.1029/2022gl099880

Barnhart, K. R., Overeem, I., & Anderson, R. S. (2014). The effect of changing sea ice on the physical vulnerability of Arctic coasts. *The Cryosphere*, *8*(5), 1777–1799. https://doi.org/10.5194/tc-8-1777-2014

Bidlot, J.-R. (2012). Present status of wave forecasting at ECMWF. In *Workshop on ocean waves* (pp. 1–17).

Castro, A. F. P., Schmandt, B., Baker, M. B., & Abbott, R. E. (2023). Tracking local sea ice extent in the Beaufort sea using distributed acoustic sensing and machine learning. *The Seismic Record*, *3*(3), 200–209. https://doi.org/10.1785/0320230019

Cheng, S., Rogers, W. E., Thomson, J., Smith, M., Doble, M. J., Wadhams, P., et al. (2017). Calibrating a viscoelastic sea ice model for wave propagation in the Arctic fall marginal ice zone. *Journal of Geophysical Research: Oceans*, *122*(11), 8770–8793. https://doi.org/10.1002/2017jc013275

Cohn, N., Bosche, L. V., Midgley, T., Small, C., Douglas, T. A., & King, J. (2022). Assessing drivers of coastal tundra retreat at point hope, Alaska. *Journal of Geophysical Research: Earth Surface*, *127*(11), e2022JF006813. https://doi.org/10.1029/2022jf006813

Herbers, T. H. C., Jessen, P. F., Janssen, T. T., Colbert, D. B., & MacMahan, J. H. (2012). Observing ocean surface waves with GPS-tracked buoys. *Journal of Atmospheric and Oceanic Technology*, *29*(7), 944–959. https://doi.org/10.1175/JTECH-D-11-00128.1

Hersbach, H., Bell, B., Berrisford, P., Hirahara, S., Horányi, A., Muñoz-Sabater, J., et al. (2020). The ERA5 global reanalysis. *Quarterly Journal of the Royal Meteorological Society*, *146*(730), 1999–2049. https://doi.org/10.1002/qj.3803

Hošeková, L., Eidam, E., Panteleev, G., Rainville, L., Rogers, W. E., & Thomson, J. (2021). Landfast ice and coastal wave exposure in northern Alaska. *Geophysical Research Letters*, *48*(22), e2021GL095103. https://doi.org/10.1029/2021gl095103

Hošeková, L., Malila, M. P., Rogers, W. E., Roach, L. A., Eidam, E., Rainville, L., et al. (2020). Attenuation of ocean surface waves in pancake and Frazil sea ice along the coast of the Chukchi sea. *Journal of Geophysical Research: Oceans*, *125*(12), e2020JC016746. https://doi.org/10.1029/2020jc016746

Kohout, A. L., & Meylan, M. H. (2008). An elastic plate model for wave attenuation and ice floe breaking in the marginal ice zone. *Journal of Geophysical Research*, *113*(C9), C09016. https://doi.org/10.1029/2007JC004434

Kohout, A. L., Smith, M., Roach, L. A., Williams, G., Montiel, F., & Williams, M. J. (2020). Observations of exponential wave attenuation in Antarctic sea ice during the pipers campaign. *Annals of Glaciology*, *61*(82), 196–209. https://doi.org/10.1017/aog.2020.36

Landrø, M., Bouffaut, L., Kriesell, H. J., Potter, J. R., Rørstadbotnen, R. A., Taweesintananon, K., et al. (2022). Sensing whales, storms, ships and earthquakes using an Arctic fibre optic cable. *Scientific Reports*, *12*(1), 19226. https://doi.org/10.1038/s41598-022-23606-x

Lindsey, N. J., Dawe, T. C., & Ajo-Franklin, J. B. (2019). Illuminating seafloor faults and ocean dynamics with dark fiber distributed acoustic sensing. *Science*, *366*(6469), 1103–1107. https://doi.org/10.1126/science.aay5881

Liu, P. C. (1989). On the slope of the equilibrium range in the frequency spectrum of wind waves. *Journal of Geophysical Research*, *94*(C4), 5017–5023. https://doi.org/10.1029/jc094ic04p05017

Lund, B., Graber, H. C., Smith, M., Doble, M., Persson, O., Thomson, J., & Wadhams, P. (2018). Arctic sea ice drift measured by shipboard marine radar. *Journal of Geophysical Research: Oceans*, *123*(6), 4298–4321. https://doi.org/10.1029/2018JC013769

Mahoney, A. (2018). Landfast sea ice in a changing Arctic. *Arctic Report Card*, *2018*, 99.

Mahoney, A., Eicken, H., Gaylord, A. G., & Gens, R. (2014). Landfast sea ice extent in the Chukchi and Beaufort seas: The annual cycle and decadal variability. *Cold Regions Science and Technology*, *103*, 41–56. https://doi.org/10.1016/j.coldregions.2014.03.003

Meylan, M. H., Bennetts, L. G., Mosig, J., Rogers, W., Doble, M., & Peter, M. A. (2018). Dispersion relations, power laws, and energy loss for waves in the marginal ice zone. *Journal of Geophysical Research: Oceans*, *123*(5), 3322–3335. https://doi.org/10.1002/2018jc013776

Rogers, W. E., Meylan, M. H., & Kohout, A. L. (2021). Estimates of spectral wave attenuation in Antarctic sea ice, using model/data inversion. *Cold Regions Science and Technology*, *182*, 103198. https://doi.org/10.1016/j.coldregions.2020.103198

Sidenko, E., Tertyshnikov, K., Lebedev, M., & Pevzner, R. (2022). Experimental study of temperature change effect on distributed acoustic sensing continuous measurements. *Geophysics*, *87*(3), D111–D122. https://doi.org/10.1190/geo2021-0524.1

Smith, M., Thomson, J., Abbott, R., & Baker, M. (2023). Ocean surface gravity wave parameters derived from seafloor DAS near Oliktok Point, Alaska, 2021-2022 [Dataset]. NSF Arctic Data Center. https://doi.org/10.18739/A2PK0736C

Squire, V. A. (2019). Ocean wave interactions with sea ice: A 2019 reappraisal. *Annu. Rev. Fluid Mech., AA*, 1–25.

Squire, V. A., & Moore, S. C. (1980). Direct measurement of the attenuation of ocean waves by pack ice. *Nature*, *283*(5745), 365–368. https://doi.org/10.1038/283365a0

Thomson, J. (2012). Wave breaking dissipation observed with "SWIFT" drifters. *Journal of Atmospheric and Oceanic Technology*, *29*(12), 1866–1882. https://doi.org/10.1175/JTECH-D-12-00018.1

Thomson, J. (2022). Wave propagation in the marginal ice zone: Connections and feedback mechanisms within the air–ice–ocean system. *Philosophical Transactions of the Royal Society A*, *380*(2235), 20210251. https://doi.org/10.1098/rsta.2021.0251

Thomson, J., Eidam, E., Hosekova, L., de Klerk, A., Roth, E., Roberts, S., & Naber, D. (2020). Coda cruise report. r/v sikuliaq. (Tech. Rep.). Retrieved from https://www.apl.washington.edu/project/projects/coda/pdfs/cruise_report_2020.pdf

Thomson, J., Girton, J. B., Jha, R., & Trapani, A. (2018). Measurements of directional wave spectra and wind stress from a wave glider autonomous surface vehicle. *Journal of Atmospheric and Oceanic Technology*, *35*(2), 347–363. https://doi.org/10.1175/jtech-d-17-0091.1

Thomson, J., Hošeková, L., Meylan, M. H., Kohout, A. L., & Kumar, N. (2021). Spurious rollover of wave attenuation rates in sea ice caused by noise in field measurements. *Journal of Geophysical Research: Oceans*, *126*(3), e2020JC016606. https://doi.org/10.1029/2020jc016606

Thomson, J., Lund, B., Hargrove, J., Smith, M. M., Horstmann, J., & MacKinnon, J. A. (2021a). Wave-driven flow along a compact marginal ice zone. *Geophysical Research Letters*, *48*(3), e2020GL090735. https://doi.org/10.1029/2020gl090735

Thomson, J., Lund, B., Hargrove, J., Smith, M. M., Horstmann, J., & MacKinnon, J. A. (2021b). Wave-driven flow along a compact marginal ice zone. *Geophysical Research Letters*, *48*(3), e2020GL090735. https://doi.org/10.1029/2020gl090735

Thomson, J., & Rogers, W. E. (2014). Swell and sea in the emerging arctic ocean. *Geophysical Research Letters*, *14*(9), 3136–3140. https://doi.org/10.1002/2014GL059983

Voermans, J. J., Babanin, A. V., Thomson, J., Smith, M. M., & Shen, H. H. (2019). Wave attenuation by sea ice turbulence. *Geophysical Research Letters*, *46*(12), 6796–6803. https://doi.org/10.1029/2019gl082945

Wadhams, P. (1983). A mechanism for the formation of ice edge bands. *Journal of Geophysical Research*, *88*(C5), 2813–2818. https://doi.org/10.1029/jc088ic05p02813

Wahlgren, S., Thomson, J., Biddle, L. C., & Swart, S. (2023). Direct observations of wave-sea ice interactions in the Antarctic Marginal Ice Zone. *ESS Open Archive*. https://doi.org/10.22541/essoar.168201718.84053333/v1

Waseda, T., Alberello, A., Nose, T., Toyota, T., Kodaira, T., & Fujiwara, Y. (2022). Observation of anomalous spectral downshifting of waves in the Okhotsk sea marginal ice zone. *Philosophical Transactions of the Royal Society A*, *380*(2235), 20210256. https://doi.org/10.1098/rsta.2021.0256

Wilcock, W. S., Abadi, S., & Lipovsky, B. P. (2023). Distributed acoustic sensing recordings of low-frequency whale calls and ship noise offshore central Oregon. *JASA Express Letters*, *3*(2), 026002. https://doi.org/10.1121/10.0017104

Williams, E. F., Fernández-Ruiz, M. R., Magalhaes, R., Vanthillo, R., Zhan, Z., González-Herráez, M., & Martins, H. F. (2019). Distributed sensing of microseisms and teleseisms with submarine dark fibers. *Nature Communications*, *10*(1), 1–11. https://doi.org/10.1038/s41467-019-13262-7